Proceedings of 8th Windsor Conference: ***Counting the Cost of Comfort in a changing world*** Cumberland Lodge, Windsor, UK, 10-13 April 2014. London: Network for Comfort and Energy Use in Buildings, http://nceub.org.uk

Study on Evaluation of Effects of Inhomogeneous Radiant Environment for Pedestrian in Summer Season using a Coupled Numerical Simulation based on CFD Analysis

Shinji Yoshida[1], Taiki Sato[2], and Masayuki Oguro[3]

1 University of Fukui, 3-9-1 Bunkyo, Fukui-city, Fukui, Japan, y-shinji@u-fukui.ac.jp;
2 Taisei Corporation, 344-1 Nase, Tozuka, Yokohama, Kanagawa, Japan, stutik00@pub.taisei.co.jp;
3 Taisei Corporation, 344-1 Nase, Tozuka, Yokohama, Kanagawa, Japan, masayuki.oguro@sakura.taisei.co.jp

Abstract

In this paper, we propose a new calculation method for evaluating the inhomogeneous outdoor thermal environment by incorporating a multi-node human thermoregulation model into the simulation method based on CFD analysis of the outdoor thermal environment. We also investigated the effects of weather conditions on the inhomogeneity of the radiant environment and the thermal comfort for pedestrians using the proposed calculation method. Two different weather condition cases are investigated in this study: (1) a scorching hot day and (2) a cloudy day. The multi-node thermoregulation model "JOS" is used in this analysis to investigate the inhomogeneity of the outdoor thermal environment. The analysis confirmed the effectiveness of the proposed method in the evaluation of the inhomogeneity of the thermal comfort in outdoor space.

Keywords: Numerical analysis, Thermoregulation model, Outdoor space, Radiation, Virtual sphere

1 Introduction

In recent years, urbanization has spread all over the world, including Japan, modifying the geometry and land use of the natural environment to that of a built environment. Urbanization alters the surface energy balance of the urban canopy and results in extensive anthropogenic heat release from various sources such as air-conditioners and cars. In Japanese cities, these changes cause the degradation of the outdoor thermal environment during the summer season, in the form of rising air and surface temperatures, weakening wind velocity, etc. This degradation has caused numerous environmental problems including an increase in the risk of heatstroke. Various countermeasures to these problems have been proposed and implemented, such as roadside planting, roof greening, and use of high albedo (reflectivity of solar radiation) paints and water-permeable materials. However, the effectiveness of such countermeasures has not been clearly confirmed. Hence, it is necessary to propose an assessment method to evaluate the effects of the countermeasures against environmental problems.

For this purpose, numerous researchers, including the present authors, have proposed several methods based on the coupled CFD analysis for evaluating outdoor thermal environment. Bouyer et al. (2007) calculated the physiological equivalent temperature

(PET) (Mayer and Höppe, 2008) spatially using the coupled effect of solar radiation, wind flow around obstructions, convective heat transfer from surfaces, and long wave radiation. Bruse (1999) proposed the ENVI-met system, which is based on a numerical meteorological model (1.5 order closure turbulent model based on the work of Mellor and Yamada (1975)) and also analysed outdoor thermal comfort and open space usage with the multi-agent system, which is based on ENVI-met (cf. Bruse, 2009). The present authors have also proposed a coupled simulation method based on computational fluid dynamics (CFD) for predicting the thermal comfort in an outdoor space, with consideration of the effect of thermal environmental conditions such as wind velocity, temperature, humidity, and radiation (Yoshida et al., 2000). Using this method, Yoshida et al. (2006) have also evaluated the effects of various types of green areas on the outdoor thermal environment.

At present, the numerical analysis method has certain drawbacks in that it is difficult to incorporate unsteady and inhomogeneous factors, which include physical environmental factors (instantaneous changes and local distributions of environmental conditions such as solar radiation and wind) and pedestrian activity factors (walking speed, rest time, activity level, and body posture), into the method for the evaluation of outdoor thermal comfort. However, the two-node cylindrical or prismatic human thermoregulation model, which was proposed by Gagge et al. (1986) and is incorporated into the abovementioned numerical analysis method, does not enable us to evaluate the effects of unsteady and inhomogeneous environmental factors on outdoor thermal comfort.

In this study, we propose a method for evaluating the inhomogeneous outdoor thermal environment by incorporating a multi-node human thermoregulation model into the simulation method based on CFD analysis of the outdoor thermal environment. In this paper, we first outline the numerical analysis method, focusing specifically on the details of the radiant computation method. Next, we introduce an application example of this calculation method for the practical evaluation of the outdoor thermal environment during the summer season. This analysis focuses on the investigation of the effects of weather on the inhomogeneity of the radiant environment and the thermal comfort for pedestrians.

2 Outline of method for evaluating outdoor thermal environment

Figure 1 outlines the computational method used for analysing the outdoor thermal environment. Boundary conditions for the CFD analysis coupled with convection and radiation are determined using the input data, as shown in Fig. 1, i.e., meteorological and geometrical data and surface conditions. The spatial distributions of wind velocity, air temperature, radiation, and humidity are estimated using the CFD-analysis-imposed boundary conditions determined using the input data. Outdoor thermal comfort, including unsteady and inhomogeneous factors, is evaluated using the multi-node human thermoregulation model on the results of the CFD analysis.

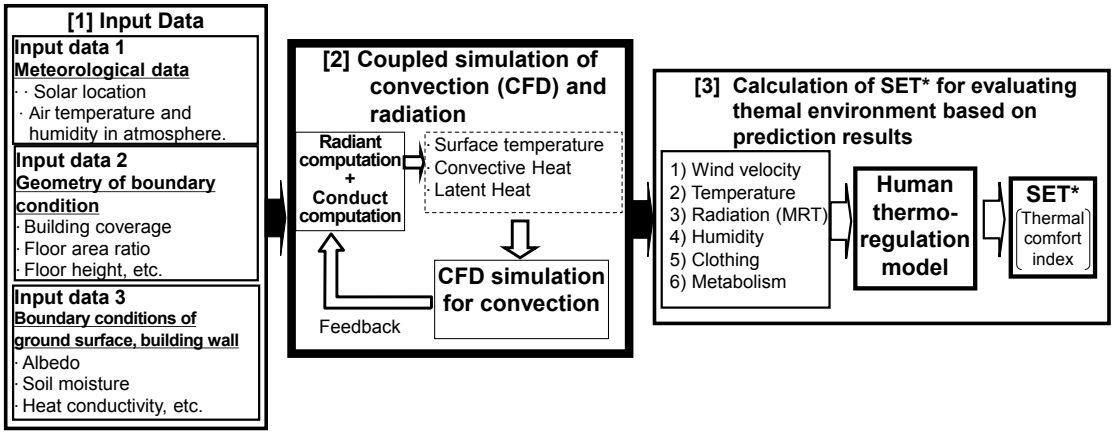

Figure 1. Flowchart for assessing outdoor thermal comfort based on CFD

3 Outline of method for calculating spatial distribution of radiant conditions in outdoor space

Before the calculation of distributions of the mean radiant temperature on each node composing the multi-node thermoregulation model, the spatial distribution of radiant conditions in the outdoor space should be obtained. This section outlines the method of the radiation calculation in the outdoor space. The outline of the method for evaluating the inhomogeneity of a radiant condition is described in the next section.

3.1 Coordinate system

Figure 2 illustrates an example of the coordinate system in an outdoor space. The surfaces of obstacles and the space are divided into small grids into which physical properties and temperature can be considered uniform.

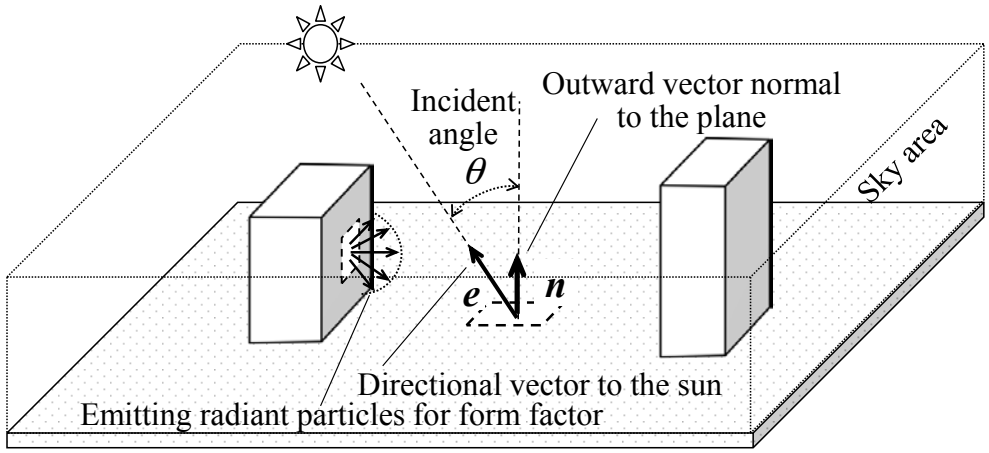

Figure 2. Outdoor coordinate system

3.2 Calculation of form factor using the Monte Carlo method

The Monte Carlo method is used in this study to calculate the form factor. For the details of this calculation method, refer to Omori et al. (1990). A large number of particles, N_{iTotal}, are emitted along the direction determined by Lambert's law from randomly selected points within a surface element i comprising the computational domain. Let N_{ij} be the number of radiant bundles that reach a surface element j.

Division of N_{ij} by N_{iTotal} provides the form factor, or the fraction of radiation leaving i that is intercepted by j, F_{ij}, as shown in Equation (1):

$$F_{ij} = N_{ij}/N_{iTotal}. \quad (1)$$

3.3 Calculation of irradiation ratio

A large number of particles are emitted from the surface element i comprising the computational domain toward the sun; these particles are used to determine whether the sun's rays reach the surface element. Let $\boldsymbol{e}$ be the unit directional vector toward the sun from the point, and $\boldsymbol{n}$ be the unit outward vector normal to the plane in which the point is included, as shown in Fig. 2. The vector $\boldsymbol{e}$ is determined using the solar altitude and azimuth, which are given by the latitude and longitude of the study area and month-day-time. When Equation (2) is satisfied, the sun's rays can reach i when there are no obstacles around the surface:

$$\boldsymbol{e} \cdot \boldsymbol{n} = cos\theta > 0, \quad (2)$$

where θ is the incident angle of the sun's ray to the plane. The particle trajectory is traced to determine whether it reaches the sky area or is intercepted by a surrounding obstacle, such as a building. The former case results in solar irradiation, and the latter in shade. This confirmation repeats a large number of times by randomly changing the emitting point within i. Then, the irradiation ratio γ_i is calculated using Equation (3) as follows:

$$\gamma_i = N_i/N_{iTotal}, \quad (3)$$

where N_i is the number of particles reaching the sky area from i.

3.4 Calculation of heat balance on the ground surface and outside a building

The distributions of the surface temperature T_i at each point are obtained using a heat balance equation at the surface of the ground and outside a building. Let S_i, R_i, H_i, D_i, and LE_i be the absorbed solar radiation gain to a surface i [W], the long-wave radiation gain to i [W], the convection heat transmission at i [W], the conduction to the building or ground [W], and the heat dissipation by evaporation from i [W], respectively. The heat balance equation consists of these elements, as shown in Equation (4):

$$S_i + R_i + H_i + D_i + LE_i = 0. \quad (4)$$

On the left side of Equation (4), a positive value indicates the inflow of energy to i, while a negative value indicates the outflow of energy. The equations for calculating each item in the Equation (4) are expressed as follows.

The absorbed solar radiation gain to i, S_i [W] is calculated using the following equations:

$$S_i = (\alpha_{i\theta} E_{Di} + \alpha_i E_{Si}) + \alpha_i \left(\sum_{j=1}^{N} F_{ji} R_{Sj}\right), \quad (5)$$

$$R_{Si} = (\rho_{i\theta} E_{Di} + \rho_i E_{Si}) + \rho_i \left(\sum_{j=1}^{N} F_{ji} R_{Sj}\right), \quad (6)$$

$$S_{Ti} = (\tau_{i\theta} E_{Di} + \tau_i E_{Si}) + \tau_i \left(\sum_{j=1}^{N} F_{ji} R_{Sj}\right), \quad (7)$$

$$E_{Di} = A_i \gamma_i I_N cos\theta, \quad (8)$$

$$E_{Si} = A_i F_{iS} I_{SH}, \quad (9)$$

where A_i is the area of i and E_{Di} and E_{Si} are the direct and sky solar radiation gains to grid i [W], respectively. Further, F_{iS} is the form factor from i to the sky, I_N is the direct

solar radiation incident on a normal surface [W], I_{SH} is the sky solar radiation incident on a horizontal surface [W], R_{Si} is the short-wave radiosity or the total short-wave radiation energy flux of a surface per unit area and unit time at i [W], S_{Ti} is the transmitted solar radiation at i [W]. The symbols α_i, ρ_i, and τ_i denote the absorptance, the reflectance, and the transmittance of solar radiation to i, and these values also include ratio of window to the surface.

The long-wave radiation gain to i, R_i [W] is calculated using the following equations:

$$R_i = \varepsilon_i E_i + \varepsilon_i \sum_{j=1}^{N} F_{ji} R_{Lj}, \tag{10}$$

$$R_{Li} = (1 - \varepsilon_i) E_i + (1 - \varepsilon_i) \sum_{j=1}^{N} F_{ji} R_{Lj}, \tag{11}$$

$$E_i = A_i \sigma T_i^4, \tag{12}$$

where E_i is the long-wave radiation emitted at i [W], R_{Li} is a long-wave radiosity at i [W], ε_i is the absorption rate of long-wave radiation of i, σ is the Stephan-Boltzmann constant [W/(m^{2}K^4)] (=5.67×10^{-8}W/(m^{2}K^4)).

The mean radiant temperature (MRT) for pedestrians is calculated using R_{Si} and R_{Li}, as we will describe later.

H_i is calculated using Equation (13).

$$H_i = A_i \alpha_C (T_{ai} - T_i), \tag{13}$$

where T_{ai} is the air temperature in the region adjacent to i [K] and α_C is the convective heat transfer coefficient [W/(m^{2}K)].

D_i is calculated using Equation (14).

$$D_i = -A_i \lambda (T_i - T_{bi}) / \Delta z, \tag{14}$$

where λ is the heat conductivity of the building material or ground, and T_{bi} is the inside wall or underground temperature at depth Δz, derived by solving the transient heat conduction problem in the solid.

LE_i is calculated using Equation (15).

$$LE_i = A_i L \alpha_W \beta_i (f_a - f_{Si}), \tag{15}$$

where f_a is the water vapour pressure at the region adjacent to i [kPa], f_{Si} is the saturated water vapour pressure at i [kPa], L is the latent heat of evaporation [J/kg], α_W is the moisture transfer coefficient [kg/(m^2·s·kPa)], and β_i is the moisture availability at i.

3.5 Calculation of air-conditioning heat load

For the analysis, discussed later in the paper, the computational domain does not include any building in order to evaluate the individual effect of weather conditions on the inhomogeneity of thermal environment for pedestrians. Hence, the air-conditioning heat load is not calculated in the present analysis. However, this calculation is obviously performed in an actual analysis in the city block. Let Q be the air-condition heat load [W]; Q consists of the heat gain through the wall Q_C [W], the solar radiation gain by penetration through windows Q_S [W], the ventilation heat gain Q_a [W], and the internal heat generation in a building Q_H [W], as described in Equation (16):

$$Q = Q_C + Q_S + Q_a + Q_H. \tag{16}$$

In this equation, a positive value indicates the inflow of energy to the building, and a negative value indicates the outflow. The equations for calculating each item in the Equation (16) are expressed as follows.

Q_C is calculated using Equation (17).

$$Q_C = \sum_{i=1}^{m} A_i \alpha_I (T_{si} - T_r), \quad (17)$$

where m is the number of surface elements comprising each building, T_r is the indoor temperature [K], T_{si} is the indoor surface wall temperature of the wall at the surface element i comprising inner walls of each building [K], and α_I is the indoor overall (convective + radiative) heat transfer coefficient [W/(m^{2}K)]. T_{si} is obtained by solving Equation (18), which is an unsteady one-dimensional heat conduction equation in the wall.

$$\rho_W C_{pW} (\partial T_{wall}/\partial t) = -(\partial q_{wall}/\partial x), \quad (18)$$

$$q_{wall} = -\lambda (\partial T_{wall}/\partial x), \quad (19)$$

where T_{wall} is the inner temperature of the wall [K]. The symbols C_{pW}, λ, and ρ_W denote the specific heat [J/(kg·K)], the heat conductivity [W/(m·K)], and the density [kg/m^3] of the material, respectively.

Q_S is calculated using Equation (20).

$$Q_S = \sum_{i=1}^{m} S_{Ti}. \quad (20)$$

Q_a is calculated using Equation (21).

$$Q_a = \rho_a \Delta i q_a, \quad (21)$$

where q_a is the amount of ventilation [m^3/s], Δi is the enthalpy difference between indoor and outdoor [J/kg], and ρ_a is the density of the air [kg/m^3].

Q_H is set to an assumed value.

When the room is air-conditioned, the heat released from the outdoor air-conditioning unit system, A_G is calculated using Equation (22). This value is used as the heat source conditions in the CFD analysis.

$$A_G = Q\,(1 + COP)/COP, \quad (22)$$

where COP is the coefficient of performance of the air-conditioning system.

4 Outline of the method for analysing inhomogeneous radiation in outdoor spaces

The objective of this study is to incorporate multi-node human thermoregulation models into the abovementioned method in order to evaluate various types of environmental designs for an outdoor space such as a relaxation space in a park and a pedestrian space on a street. A pedestrian in the park and street continually changes walking speed, activity level, posture, and facing direction. These factors instantaneously affect wind and radiant conditions around each segment of the pedestrian's body. Hence, it is necessary to provide environmental conditions together with a relationship between disposition and direction of the thermoregulation model in a computational domain. In this section, we outline the method used to analyse the inhomogeneity of radiant conditions in outdoor spaces.

4.1 Virtual spheres centred on human body

It is necessary to analyse incident short- and long-wave radiation from all directions around the pedestrian in order to include the effects of inhomogeneity on radiation. The method described in this paper is used to calculate the incident radiations on each segment of the thermoregulation model through the surface of a virtual sphere centred on the model. Fig. 3 illustrates the virtual sphere centred on a human body. Spatial distributions of solar and long-wave radiation in the computational domain are calculated on each mesh for the analysis of the outdoor thermal environment, as mentioned above. On each mesh, we consider that a virtual sphere is centred on a human body; the sphere's surface is divided into 266 with each element being 15° in both azimuth and altitude.

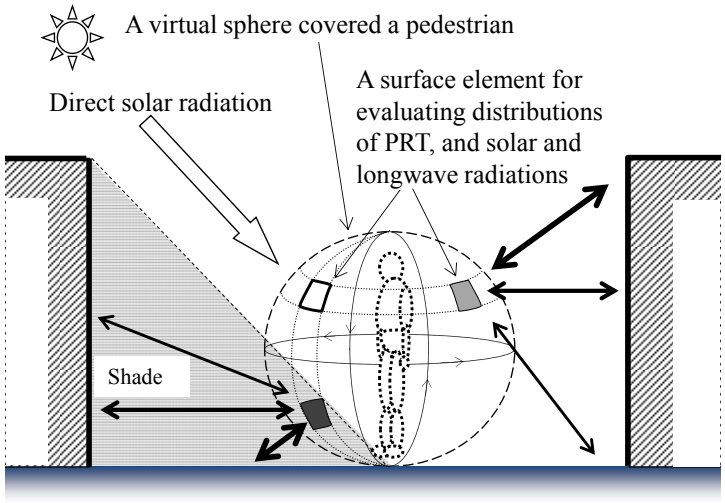

Figure 3. Conceptual figure of virtual sphere centring around a human body.

4.2 Plane radiant temperature and solar irradiation on each surface element comprising the virtual sphere surface

Short- and long-wave radiation and plane radiant temperature (PRT) on each surface element comprising the virtual sphere surface are calculated using the same manner of the radiant analysis method described in the previous section. The plane radiant temperature on each surface element *i* comprising the virtual sphere surface, $T_{Vprt\text{-}i}$, is calculated using Equation (23) as follows:

$$A_{Vi}\sigma T_{Vprt-i}^{4} = \sum_{j=1}^{n} F_{ji}R_{Lj}. \quad (23)$$

In this equation, A_{Vi} is the area of a surface element *i*, which comprises the virtual sphere surface [m^2], R_{Lj} is the long-wave radiosity at the surface element *j*, which comprises the computational domain [W], and is obtained by Equation (10).

The solar radiation reaching *i*, S_{Vi} [W], is calculated using Equations (24), (25), and (26) as follows:

$$S_{Vi} = E_{VDi} + E_{VSi} + \sum_{j=1}^{n} F_{ji}S_{Rj}, \quad (24)$$

$$E_{VDi} = A_{Vi}\gamma_i I_N cos\theta, \quad (25)$$

$$E_{VSi} = A_{Vi}F_{iS}I_{SH}. \quad (26)$$

In this equation, E_{VDi} and E_{VSi} are the direct and sky solar radiation gains to *i* [W], respectively. Further, R_{Sj} is the short-wave radiosity at the surface element *j* comprising the computational domain [W] by Equation (6).

4.3 Short- and long-wave radiation, MRT in each segment of the thermoregulation model

Absorbed short- and long-wave radiation, S_{seg} and R_{seg}, and the mean radiant temperature (MRT), $T_{prt\text{-}seg}$, in each segment of thermoregulation model are calculated using Equations (27), (28), and (29) as follows:

$$R_{seg} = \left(\sum_{i=1}^{n_{surf}} A_{Vi}\sigma T_{Vprt-i}^{4} f_{pi}\right)/\pi, \quad (27)$$

$$S_{seg} = \left(\sum_{i=1}^{n_{surf}} \alpha_{seg-i} S_{Vi} f_i\right)/\pi, \quad (28)$$

$$T_{mrt-seg} = \left[\left(R_{seg} + S_{seg}\right)/\sigma\right]^{1/4}, \quad (29)$$

where $\alpha_{seg\text{-}i}$ is the absorption rate of solar radiation to i including the virtual sphere surface, f_{pi} is the projected area factor between each segment of the model and i. The disposition and direction of the virtual sphere centring the human thermoregulation model is associated with the projected area factor, which enables us to consider the inhomogeneous condition including the effect of a pedestrian's direction on a radiant environment.

The projected area factor (Fanger et al., 1970) has been used as an analysis method of the form factor between the entire human body and the surrounding walls in various studies concerning the radiant environment in indoor and outdoor spaces. In the recent study, we have expanded the method of projected area factor to each part of the body by dividing the body into 17 parts, and quickly developed the databases using a 3D model of the human body (Sato et al., 2014). Figure 4 illustrates an example of f_{pi} on the chest segment. Figure 5 also compares the form factor of each body segment to each surface comprising the computational domain by the method based on projected area factor with the direct calculation with differential areas of the body surface. We can see that the results with the projected area factor agree well with that with the direct calculation. The length of the domain in Fig. 5 is very close to the radius of the virtual sphere; therefore, the results become helpful in estimation of accuracy of the calculation method with the virtual sphere.

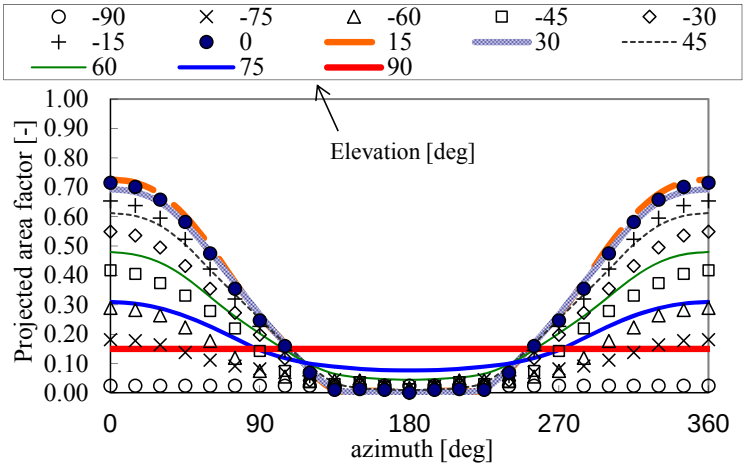

Figure 4. Projected area factor distribution for the chest segment.

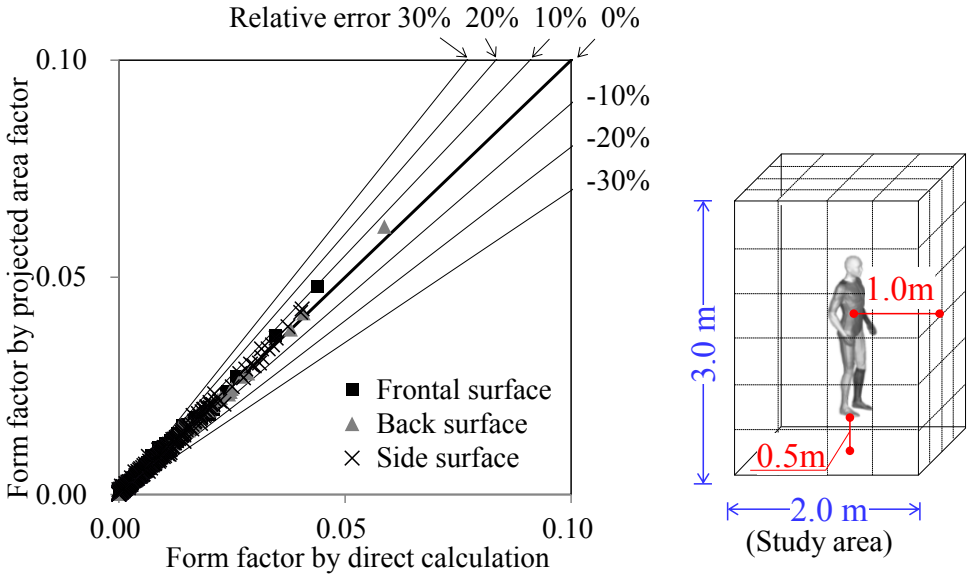

Figure 5. Comparison between the form factor by projected area factor and that by direct calculation.

5 Outline of method for including the inhomogeneous effect of airflow on thermal environments

The inhomogeneity of airflow affects convective heat transfer coefficients and clothing insulations on each segment of the human thermoregulation model.

The convective heat transfer coefficient on each segment of the thermoregulation model includes a relationship between the direction the pedestrian is facing and the airflow, as evaluated either upwind or downstream. The coefficient h_c [W/(m^{2}K)] is determined using Equation (30) as follows:

$$h_c = a \cdot v^b, \tag{30}$$

where v is the relative velocity of airflow [m/s], and a and b are constants on each segment. These constants are determined using the results measured by Oguro et al. (2002). As an example, Table 1 summarizes these constants for a standing pedestrian.

Table 1. Models of convective heat transfer coefficient and clothing insulation for standing pedestrian.

Segment	Convective Heat Transfer Coefficient: $h_c = a \cdot v^b$										Clothing Insulation: $I_{cl} = a \cdot \ln(v) + b$			
	Upwind					Downstream					Upwind		Downstream	
	Nude case h_n		Clothed case h_{cl}		h_{cl}/h_n	Nude case h_n		Clothed case h_{cl}		h_{cl}/h_n	a	b	a	b
	a	b	a	b		a	b	a	b					
Whole Body	9.31	0.60	13.36	0.60	1.42	9.41	0.61	12.38	0.65	1.34	-0.090	0.632	-0.076	0.617
Head	7.14	0.65	24.07	0.68	3.40	6.52	0.69	15.11	0.68	2.32	-0.240	0.642	-0.256	0.735
Chest	7.77	0.59	13.80	0.77	1.91	5.81	0.77	6.90	0.71	1.18	-0.136	0.917	-0.060	0.946
Back	5.86	0.74	7.67	0.63	1.30	7.75	0.57	13.87	0.72	1.93	-0.090	0.861	-0.141	0.820
Pelvic Region	7.60	0.65	11.09	0.60	1.46	8.16	0.61	9.99	0.63	1.24	-0.114	1.057	-0.102	0.970
L- Shoulder	10.04	0.59	11.86	0.63	1.19	10.25	0.62	10.31	0.72	1.04	-0.097	0.566	-0.064	0.554
L-Arm	11.40	0.60	15.46	0.50	1.33	11.37	0.59	14.26	0.69	1.30	-0.096	0.579	-0.074	0.538
L-Hand	16.57	0.59	16.57	0.59	1.00	15.25	0.54	15.25	0.54	1.00				
R-Shoulder	9.51	0.62	10.62	0.70	1.14	8.99	0.63	10.17	0.74	1.18	-0.101	0.563	-0.057	0.529
R-Arm	11.79	0.57	14.61	0.57	1.25	11.05	0.61	13.78	0.66	1.27	-0.096	0.614	-0.079	0.576
R-Hand	14.04	0.57	14.04	0.57	1.00	16.66	0.52	16.66	0.52	1.00				
L-Thigh	8.94	0.58	11.02	0.53	1.23	9.19	0.63	11.80	0.57	1.28	-0.072	0.480	-0.016	0.406
L-Leg	11.70	0.54	14.80	0.52	1.26	12.42	0.55	17.32	0.64	1.42	-0.049	0.512	-0.042	0.516
L-Foot	10.59	0.53	10.59	0.53	1.00	10.87	0.60	10.87	0.60	1.00	-0.037	0.647	-0.057	0.643
R-Thigh	8.95	0.60	9.47	0.50	1.05	8.99	0.63	10.02	0.62	1.12	-0.055	0.419	-0.038	0.415
R-Leg	12.03	0.57	14.24	0.53	1.18	12.54	0.56	17.77	0.65	1.44	-0.057	0.503	-0.041	0.524
R-Foot	10.77	0.51	10.77	0.51	1.00	10.91	0.58	10.91	0.58	1.00	-0.038	0.633	-0.059	0.660

* v : velocity of airflow [m/s]

Clothing insulations on each segment vary with the thickness of the air layer between the clothing and the skin. The relationship between the pedestrian's facing direction and the airflow direction also affects the distributions of air layer thickness. Therefore, the following equation that includes the effect of the relationship on the clothing insulation [clo] on each segment is used in this study:

$$I_{cl} = a \cdot \ln v + b. \quad (31)$$

Table 1 also lists the values of the constants a and b for a standing pedestrian.

6 Outline of multi-node human thermoregulation model

The human thermoregulation model enables us to predict the thermal physiological mechanism, which regulates heat production and heat loss through vasodilation, vasoconstriction, shivering, and sweating, in order to maintain the core temperature within normal limits. Recently, a research group led by Tanabe in Waseda University in Japan developed four multi-node human thermoregulation models known as "65MN" (Tanabe et al, 2002), "COM" (Tanabe et al., 2006), "JOS" (Sato et al., 2003), and "JOS-2" (Kobayashi and Tanabe, 2013).

The calculation method proposed in this paper allows us to adopt one of these human thermoregulation models, and to replace it according to our wishes. In the analysis at the latter part of this paper, we use the JOS as the thermoregulation model since our code of the JOS-2 is now under constructing. Hence, we will change to the JOS-2 when it is complete.

The JOS model is based on Stolwijk's well-known model (Stolwijk, J.A.J., 1971). The body surface and weight for a standard body are set to 1.87 m^2 and 74.43 kg respectively. The entire body is divided into 17 body segments (head, neck, chest, back, pelvis, left shoulder, left arm, left hand, right shoulder, right arm, right hand, left thigh, left leg, left foot, right thigh, right leg, and right foot). All individual body segments consist of a core layer, a skin layer, an artery blood pool, a vein blood pool, and a superficial vein blood pool. Additionally, the JOS has arteriovenous anastomoses (AVA) that connect arteries and superficial veins without exchanging heat with any tissues in each segment of the hands and feet. For the details of the JOS, refer to the above mentioned literature (Sato et al., 2003, and Kobayashi and Tanabe, 2013).

7 Outline of convection calculation

In this calculation method, we use various types of the turbulent model of CFD analysis. In the present stage of the development of the calculation method, the standard k-ε model or the revised one allow us to use the practical analysis, and we have introduced the following two improvements to the standard model: (1) Inclusion of the effect of buoyancy on the evaluation of the turbulent-flow heat flux, such as the WET model (Launder, 1998), and (2) Inclusion of the function that controls excessive production of the turbulent-flow energy k on the building windward side, such as the modified Kato-Launder model (Kato and Launder, 1993). In this paper, we omit the explanation of details of this calculation because we mainly focus on the effect of inhomogeneous radiant condition at the analysis described below, then do not carry out the convection calculation in the present analysis. We will describe it when we

investigate the effect of inhomogeneity of wind condition on the thermal comfort for the pedestrian using this calculation method. For the details of the CFD analysis method, refer to Chen et al. (2004).

8 Outline of analysis

In this section, we investigate the effects of the weather on an inhomogeneity of a radiant environment in an outdoor space during the summer season in order to evaluate availability of the proposed method in this paper.

8.1 Study area

Figure 6 illustrates the computational domain in this analysis. It is assumed that a pedestrian stands still for long periods in the domain where no effects of complex terrain and building location are included. This is because we obtain simple calculation results for evaluating the only effect of weather conditions on inhomogeneity on a radiant environment for a pedestrian. The shape of the pedestrian is also illustrated in Fig. 6. We use a numerical shape model of a male human body, which was estimated by Ito et al., 2006. Table 2 summarizes the surface area for each segment of the human body. In this analysis, it is assumed that the clothes for the pedestrian are an office worker style during the summer season, or a white short-sleeved shirt and dark-blue trousers. The values of albedo, or reflectance of short wave radiation, for the shirt, the trousers, and the skin for the pedestrian are set to 0.6, 0.2, and 0.4, respectively. The ground in the domain is covered with concrete.

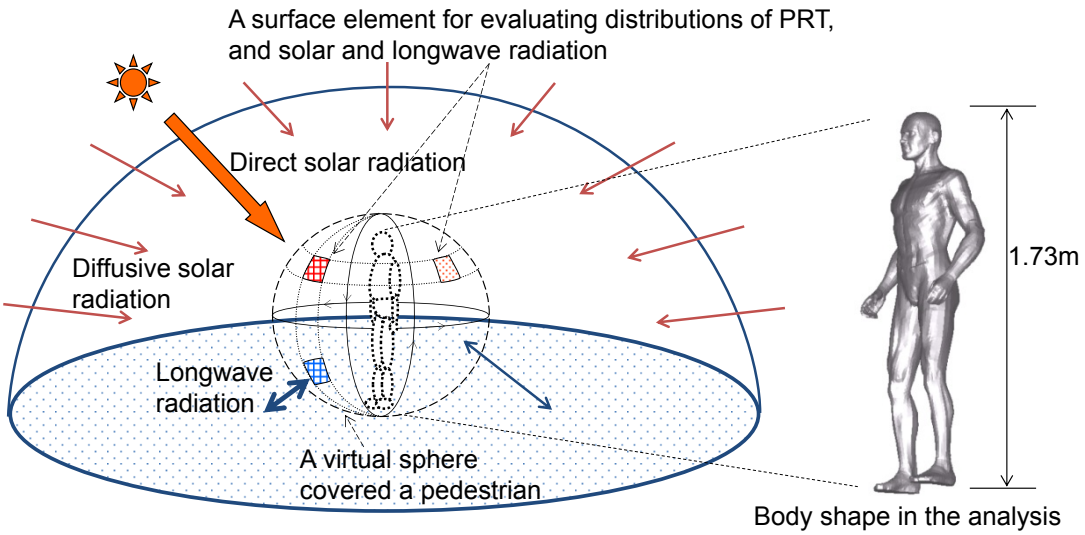

Figure 6. Computational domain in the present analysis.

Table 2. Surface area of each segment of the multi-node thermoregulation model.

No	Segment	Standard body for JOS		Surface area of each segment for the human body in the analysis [m^2]
		Surface area[m^2]	Weight [kg]	
1	Head	0.110	3.180	0.119
2	Neck	0.029	0.840	0.029
3	Chest	0.175	12.400	0.168
4	Back	0.161	11.030	0.149
5	Pelvis	0.221	17.570	0.201
6	L_Shldr	0.096	2.160	0.075
7	L_Arm	0.063	1.370	0.071
8	L_Hand	0.050	0.340	0.038
9	R_Shldr	0.096	2.160	0.075
10	R_Arm	0.063	1.370	0.071
11	R_Hand	0.050	0.340	0.038
12	L_Thigh	0.209	7.010	0.192
13	L_Leg	0.112	3.340	0.112
14	L_Foot	0.056	0.480	0.052
15	R_Thigh	0.209	7.010	0.191
16	R_Leg	0.112	3.340	0.113
17	R_Foot	0.056	0.480	0.054
	WholeBody	1.868	74.420	1.745

8.2 Computational conditions for the multi-node human thermoregulation model

In this analysis, we used the JOS model as a multi-node human thermoregulation model in order to evaluate the thermal comfort of the pedestrian. As shown in Table 2, the surface area of each body segment for the human body in the present analysis is different from the standard body shape. The heat characteristics of the human body depend on physical properties, such as posture, gender, and age, and other individual factors. Hence, in the present analysis, it is necessary to incorporate the effects of the surface area on the heat characteristics into the calculation model. The JOS enables us to include these effects on values of coefficients concerning thermoregulation mechanisms. In this study, we set these values from the literature of the JOS-2 model (Kobayashi et al., 2013).

8.3 Meteorological condition

We investigate the following two different weather conditions cases in this analysis: a scorching hot day (case 1), and a cloudy day (case 2). Meteorological data measured at the Japan Meteorological Agency in Tokyo are used in this study, and target days for case 1 and case 2 are set to 23 July and 14 August in 2010, respectively. The analysis starts at 6:00 on a day before the target day, and a time integration of 48 hours is performed using the meteorological data. The thermal environment for the pedestrian is evaluated using the results obtained at 15:00 on each target day. Figure 7 illustrates the time variations of the global solar radiation and the air temperature during the period of the computation, as an example of the meteorological data. Table 3 also summarizes the meteorological conditions at the target time for the evaluation on the outdoor thermal comfort for the pedestrian. In the present analysis, the orientation of the pedestrian is set to a south direction. Hence, it is assumed that the solar radiation irradiates from a right-hand side direction for the pedestrian.

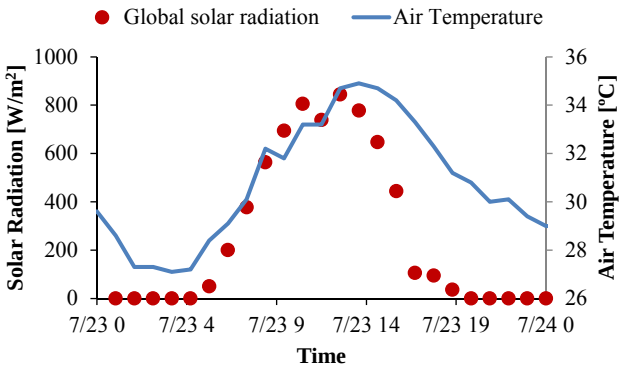

(1) case 1 (a scorching hot day, 2010/07/23)

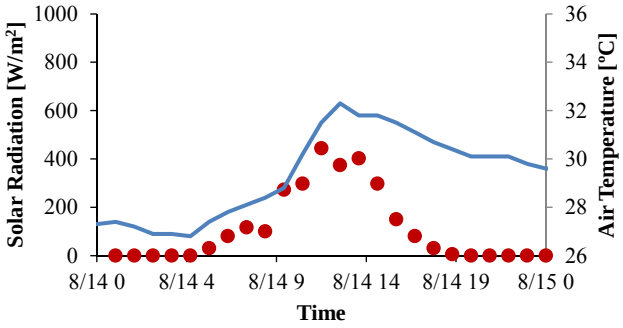

(2) case 2 (a cloudy day, 2010/08/14)

Figure 7. Time variations of global solar radiation and air temperature.

Table 3. Meteorological condition at the target time for this analysis

case	Case 1	Case 2
Target time	15:00 on 23rd July in 2010	15:00 on 14th August in 2010
Weather	A scorching hot day	A cloudy day
Global solar radiation [W/m^2]	647.2	297.2
Sun's altitude [deg]	45.1	41.7
Sun's azimuth [deg]	82.9 (nearly W)	76.6 (nearly WSW)
Air temperature [ºC]	34.7	31.8
Relative humidity [%]	48	62
Wind direction and velocity	SSE, 1.2m/s	SSW, 1.6m/s
Orientation of the pedestrian	0.0 (South)	

8.4 Computational conditions for the metabolic rate, convective heat transfer coefficients, and clothing insulation

A value of the metabolic rate and a duration time of exposure are set to 1.2 Met and one hour, respectively. Convective heat transfer coefficients and clothing insulations for each body segment are calculated using the function of wind velocity, which is proposed by Oguro et al. (2001), as mentioned in the previous section.

9 Results and discussion

9.1 MRT

Firstly, we validate accuracy of the evaluation of calculation results of MRT using the virtual sphere model, which is proposed in the present paper. Figure 8 illustrates the time variations of MRT for an entire body. Figure 9 shows a comparison of the results

of MRT using the virtual sphere (V. S.) model with the existing prismatic human body (P. B.) model (Nakamura, 1987). The values in these figures are calculated on the assumption that the short wave radiation incident to the surface of the human body is perfectly absorbed in order to eliminate the effect of colours of the clothing and the skin of the human body. In the weak inhomogeneity of radiant conditions, such as the whole day of cloudy condition and the night time on a sunny day, we can see a small difference in the results between V.S. and P.B. The results reflect the fact that the method using V.S. enables us to obtain the calculation results that have the equivalent accuracy to the results using P.B. Additionally, in the strong inhomogeneous radiant condition, or the daytime in the sunny day, we can see the MRT from V.S. is approximately 5 ºC larger than from P.B., as shown in Fig. 9. This is caused by the fact that the V.S. model can predict the inhomogeneous radiant condition accurately. Hence, from the above estimation, it has been found that the V.S. model has the adequate accuracy for the radiant computation.

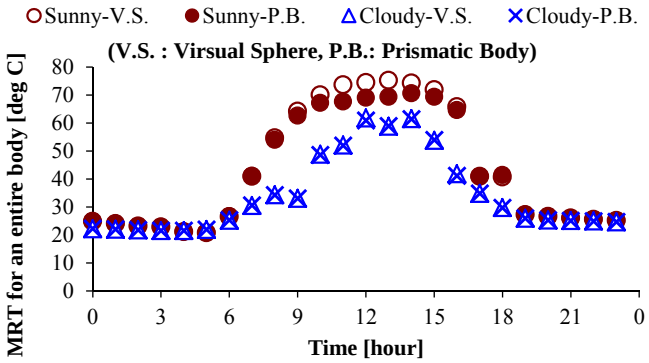

Figure 8. Time variations of MRT for a whole body.

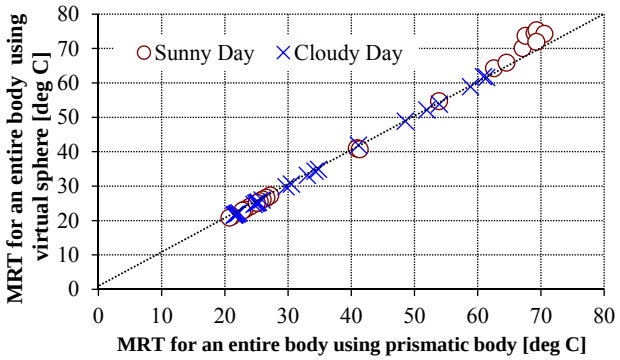

Figure 9. Comparison of MRT values for the whole body using the different calculation method.

Figure 10 illustrates the distribution of MRT on each body segment for the pedestrian. Both values in case 1–2 and case 2–2 are calculated on the same assumption in Fig. 8 and Fig. 9. Alternatively, in case 1–1 and case 2–1, it is assumed that the pedestrian wears the usual clothing style for a man in an office building during summer. As abovementioned, the orientation of the pedestrian is set to a south direction, then a solar radiation irradiates from a right-hand side direction for the pedestrian. Hence, the values in case 1–2 range from approximately 65 ºC to approximately 85 ºC, and the values on the right shoulder, the right arm, and the right hand are significantly high. While in case 2–2, or a cloudy condition, MRT on each body segment range from approximately 52–55 ºC, therefore the difference is quite small. We also see that values in case 1–1 and case 2–1 are lower than those in case 1–2 and case 2–2, respectively, and there are large differences of MRT on the upper body segments.

This difference is caused by considering effects of colours of a white short-sleeved shirt and skin on reflectance for the short-wave radiation.

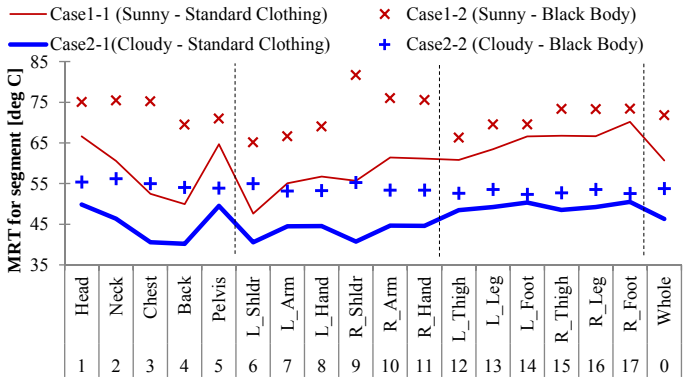

Figure 10. Distribution of MRT on each body segment for the pedestrian

9.2 Distribution of each node temperature

Figure11 illustrates the distributions of mean temperature of each node in body segments. In case1–1, or a scorching hot day, skin temperatures on the right-hand side segments are higher than those on the opposite side segments since the solar radiation irradiates to the right-hand side direction for the pedestrian. We also see a large difference of each node temperature between both cases, especially on the four limbs. This is caused by the function of the AVA on the thermal physiology in the heavy hot environment, such as case 1–1. As mentioned above, the AVA models are incorporated into the JOS model, and are located in each segment of the hands and feet. The openness percentage of the AVA, O_{AVA} varies with the thermal environment in order to control the blood flow to the surface vein blood pool using the following equations:

$$O_{AVA} = 0.265(T_{sk} - 34.0) + 0.953(T_{cr} - 36.8) + 0.9126, \quad (32)$$

$$O_{AVA} = 0.265(T_{sk} - 35.4) + 0.953(T_{cr} - 37.0) + 0.9126. \quad (33)$$

In these equations, the symbols T_{sk} and T_{cr} also denote the skin and the core temperature in each segment of the hands and feet. If the value of O_{AVA} is larger than 1 or is smaller than 0, O_{AVA} is set to 1, and 0 respectively. Figure 12 illustrates the time variations of the mean openness percentage of the AVA, which is the average between the four limbs. In case1–1 (a sunny condition), the value of O_{AVA} reaches the maximum value at 10 minutes after the beginning of the calculation. This is because a bloodstream in each limb segment increases with the hot thermal environment in order to transfer an inner heat from the core to the skin smoothly. The temperature of the blood flow from the core to skin is higher than the skin temperature. Hence, the skin temperature rises with the increase of the blood flow in four limb segments, as shown in Fig. 11. On the other hand, the value of O_{AVA} on a cloudy day falls below 0.4 at the end of the calculation, and the amount of the blood flow in the limb segments is not as large as that in case 1–1. Hence, it has been thought that the temperatures in the four limbs resulted in the low value in this analysis.

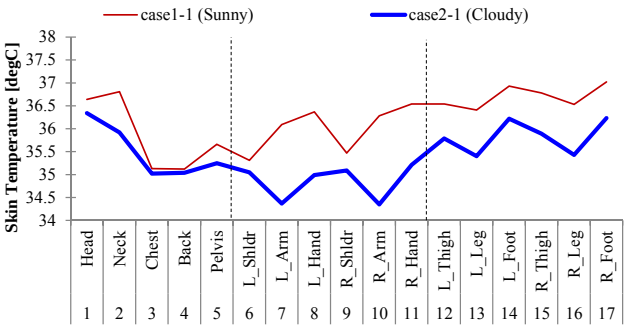

(1) Skin temperature

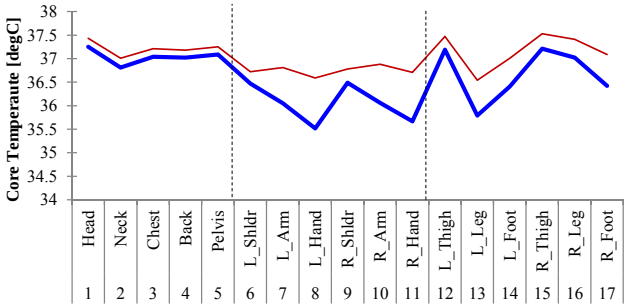

(2) Core temperature

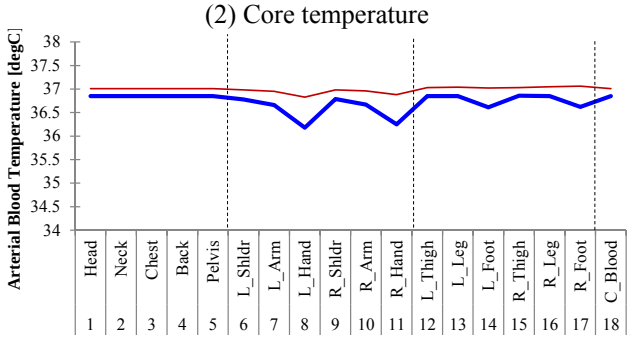

(3) Arterial blood pool temperature

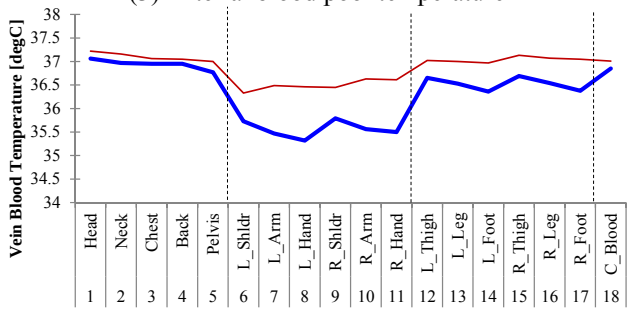

(4) Vein blood pool temperature

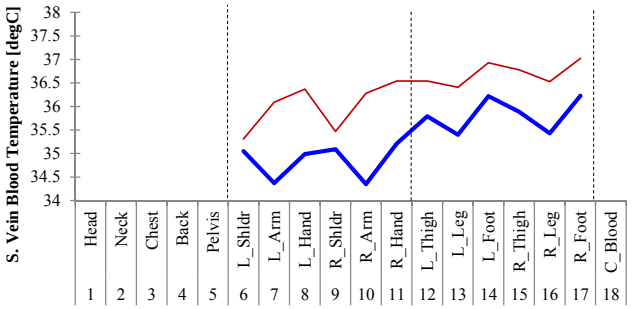

(5) Superficial vein blood pool temperature

Figure 11. Distribution of MRT on each body segment for the pedestrian

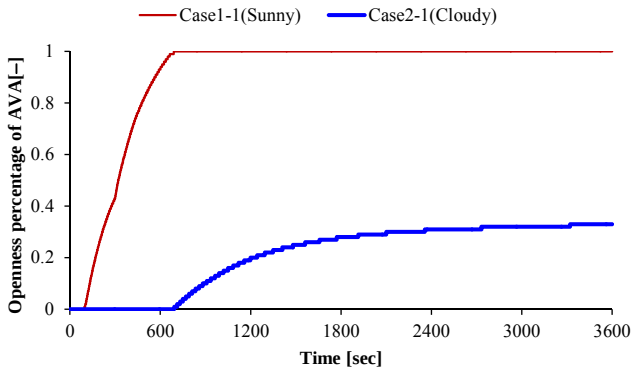

Figure 12. Time variations of mean openness percentage of the AVA

9.3 Mean skin temperature and mean core temperature for the entire body

Figure 13 shows the time variations of mean skin temperature for the entire body during the exposure time. The value in case 1–1 at the end of the calculation is approximately 36.1 °C, and that in case 2–1 is approximately 35.4°C. The value in case 1–1 is 0.7°C larger than that in case 2–1.

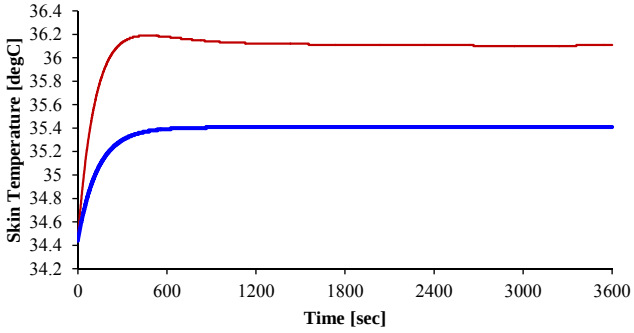

Figure 13. Time variations of mean skin temperature for the entire body.

The time variations of core temperature for the entire body are illustrated in Fig. 14. The values in both cases gradually increase with the exposure time. The value in case 1–1 at the end of the calculation is approximately 37.3 °C, and that in case 2–1 is approximately 37.0°C. The value in case 1–1 is 0.3°C larger than that in case 2–1.

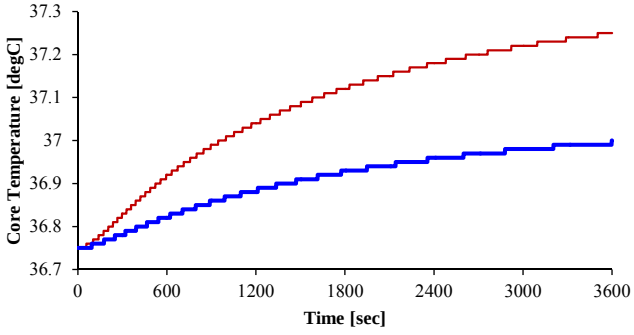

Figure 14. Time variations of mean core temperature for the entire body.

9.4 Skin wettedness and cumulative sum of regulated sweat

Figure 15 illustrates the result on skin wittedness using the thermoregulation model. The value in case 1–1 at the end of the calculation is approximately 47%, and that in case 2–1 is approximately 27%.

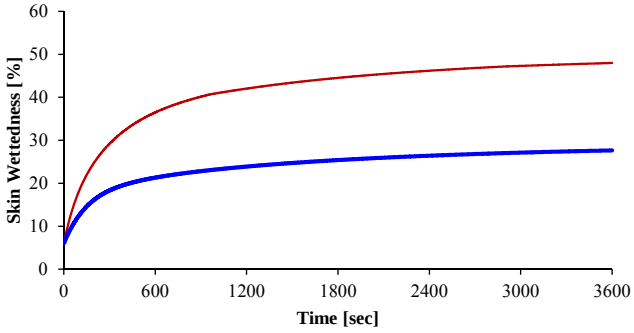

Figure 15. Time variations of mean skin wettedness for the entire body.

The time variations of the cumulative sum of the regulated sweat are shown in Fig. 16. The value in case 1–1 reached 174 g at the end of the calculation, whereas the value in case 2–1 reached 79 g. It is well known that the human body sweats in order to release additional heat to its surroundings. Hence, we can regard sweating as the result of an inner effort by the human body. It has been estimated that the intensity of the thermal load in case 2–1 is equivalent to approximately 0.45 times that in case 1–1.

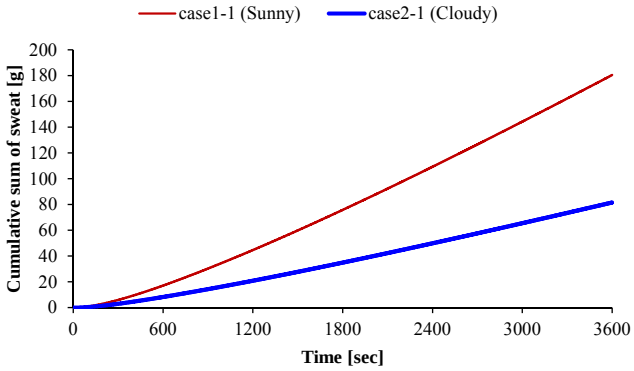

Figure 16. Time variations of cumulative sum of regulated sweat for the pedestrian.

10 Concluding remarks

(1) In this paper, we outlined a new calculation method for evaluating the inhomogeneous outdoor thermal environment by incorporating a multi-node human thermoregulation model into the simulation method based on CFD analysis of the outdoor thermal environment.

(2) In the latter part of this paper, we investigated the effects of weather on the inhomogeneity of the radiant environment and the thermal comfort for pedestrians using the proposed calculation method. In this analysis, two different weather condition cases were considered: (1) a scorching hot day and (2) a cloudy day. From the results of the analysis, it has been estimated that the intensity of the thermal load on the sunny day is approximately 2.2 times stronger than the intensity on the cloudy day.

(3) Through the investigation of the analysis, it has also been found that the proposed method in this study is a powerful tool for the evaluation of the inhomogeneity of the thermal comfort in the outdoor space. A future direction of this study will be to evaluate the effects of the inhomogeneity of wind environment on the thermal

comfort for the pedestrian in the outdoor space and to apply the calculation method to more practical assessments on thermal comfort in outdoor space.

Acknowledgement

This study was partially funded by the Grant-in-Aid for Young Scientists (B) (no.17760466, 19760403, 25820279).

References

Bouyer, J., Vinet, J., Delpech, P., and Carre, S. 2007. Thermal comfort assessment in semi-outdoor environments: Application to comfort study in stadia. *J. Wind Eng. Ind. Aerodyn.* 95, pp 963-976.

Bruse, M., 1999. Modelling and Strategies for improved urban climates. *Proceedings International Conference on Urban Climatology & International Congress of Biometeorology*, Sydney, Australia, 8-12 November 1999, http://www.envi-met.com/scidocs.htm.

Bruse, M., 2009. Analysing human outdoor thermal comfort and open space usage with the Multi-Agent System BOT world. *Seventh International Conference on Urban Climate ICUC-7*, Yokohama, Japan, 29 June – 3 July 2009, B14-3.

Chen, H., Ooka, R., Harayama, K., Kato, S., Li, X., 2004. Study on outdoor thermal environment of apartment block in Shenzhen, China with coupled simulation of convection, radiation and conduction. *Energy and Buildings,* 36, pp 1247-1258.

Fanger, P. O., Angelius, O., Kjerulf-Jensen, P., 1970. Radiation data for the human body, ASHRAE Transactions, 76, pp 338-373.

Gagge, A.P., Stolgijk, J.A.J., and Nishi, Y., 1986. A standard predictive index of human response to the thermal environment. *ASHARE Transactions*, Vol.92, part 1, pp 709-731.

Ito, K., Mukai, Y., Murakami, T., Yoshimura, J., and Hayashi T., 2008. Development of the Virtual Manikins and a Grid Library for CFD Analysis. *YSRIM 2008, Proc. of the Yellow Sea Rim International Exchange Meeting on Building Environment and Energy 2008*, Busan, Korea, 21-23 January 2008, pp 175-182.

Kato, M., Launder, B. E., 1993. The modelling of turbulent flow around stationary and vibrating square cylinders. *Prep. of the 9th Symposium on Turbulent Shear Flow*, Kyoto, Japan, 16-18 August 1993, pp 1-6.

Kobayashi, M., and Tanabe, S., 2013. Development of JOS-2 human thermoregulation modelwith detailed vascular system. *Building and Environment*, 66, pp 1-10.

Launder, B. E., 1988. On the computation of convective heat transfer in complex turbulent flows. *Trans. ASME, J. Heat Transfer*, 110, pp 1112-1128.

Mayer, H., 2008. KLIMES - a joint research project on human thermal comfort in cities. *Ber. Meteor. Inst. Univ. Freiburg*, No. 17, pp 101-117.

Mayer, H., and Höppe, 1987. Thermal comfort of man in different urban environments. *Theor. Appl. Climatol.*, 38, pp 43-49.

Mellor G. L. and Yamada, T. 1975. A simulation of the Wangara atmospheric boundary layer data. *J. Atmos. Sci.* 32, pp 2309–2329.

Nakamura, Y., 1987.Expression method of the radiant field on a human body in buildings and urban spaces. *J. Archit. Plann. Environ. Eng., AIJ*, 376, pp 29-35 (in Japanese with English abstract).

Oguro, M., Arens, E., Zhang, H., Tsuzuki, K., and Katayama, T., 2001. Measurement of projected area factors for thermal radiation analysis on each part of the human body. *J. Archit. Plann. Environ. Eng., AIJ*, 547, pp 17-25.

Oguro, M., Arens, de Dear, R., E., Zhang, H., and Katayama, T., 2002, Convective heat transfer coefficients and clothing insulations for parts of the clothed human body under airflow conditions, *J. Archit. Plann. Environ. Eng., AIJ*, 561, pp 21-29.

Oomori, T., Taniguchi, H., Kudo, K., 1990. Monte Carlo simulation of indoor radiant environment. *Int. J. Numerical Methods in Engineering*, 30(4), pp 615-627

Sato, T., Oguro, M., and Yoshida, S., 2014. Evaluation of radiative heat transfer to human body in indoor space using projected area factors for each part of human body, Part 1 Estimation of projected area factors using human shape model and evaluation of angle factors for closely located walls. *Transactions of the society of heating, air-conditioning, and sanitary engineers of Japan*, 202, pp 1-10 (in Japanese with English abstract).

Sato, T., Xu, L., Tanabe, S., 2003. Development of human thermoregulation model JOS applicable to different types of human body. *Proceedings of Healthy Buildings 2003*, Singapore, 7-11 December 2003, Vol. 1, pp 828-834.

Stolwijk, JAJ., 1971. A mathematical model of physiological temperature regulation in man, *NASA contractor report-1885*.

Tanabe, S., Kobayashi, K., Nakano, J., Ozeki Y., and Konishi, M., 2002. Evaluation of thermal comfort using combined multi-node thermoregulation (65MN) and radiation models and computational fluid dynamics (CFD). *Energy and Buildings*, 34, pp 637-646.

Tanabe, S., Kobayashi, K., and Ogawa, K., 2006. Development of numerical thermoregulation model COM for evaluation of thermal environment. *J. Environ. Eng., AIJ*, 599, pp 31-38 (in Japanese with English abstract).

Yoshida, S., Shuzo Murakami, Ryozo Ooka, Akashi Mochida, Yoshihide Tominaga, 2000. CFD prediction of thermal comfort in microscale wind climate. *Abstracts of papers presented at the 3rd International Symposium on Computational Wind Engineering,* Birmingham, U.K., 4-7 September 2000, pp 27-30.

Yoshida, S., Ooka, R., Mochida, A., Murakami, S. and Tominaga, Y., 2006. Development of three dimensional plant canopy model for numerical simulation of outdoor thermal environment. *the 6th International Conference on Urban Climate*, Göeborg, Sweden, 12-16 June 2006, pp 513-516.

Yoshida, S., Oguro, M., 2009. Investigation on a method incorporating inhomogeneous environmental conditions into CFD analysis of outdoor thermal environment coupled with multifractional human thermoregulation model. *the 7th International Conference on Urban Climate*, Yokohama, Japan, 29 June – 3 July 2009, B4.